# Shack Hartmann Subaperture Cross Coupling Study

## 1. Introduction

If one looks closely, raw centroid videos of the Shack Hartmann focal plane consistently show faint vertical and horizontal connecting lines between neighboring Hartmann spots. An example of this phenomena is shown below by the screen shot of the Arcturus data video of fc2_save_2014-04-24-000113-0000.avi , frame rate of 120 fps.

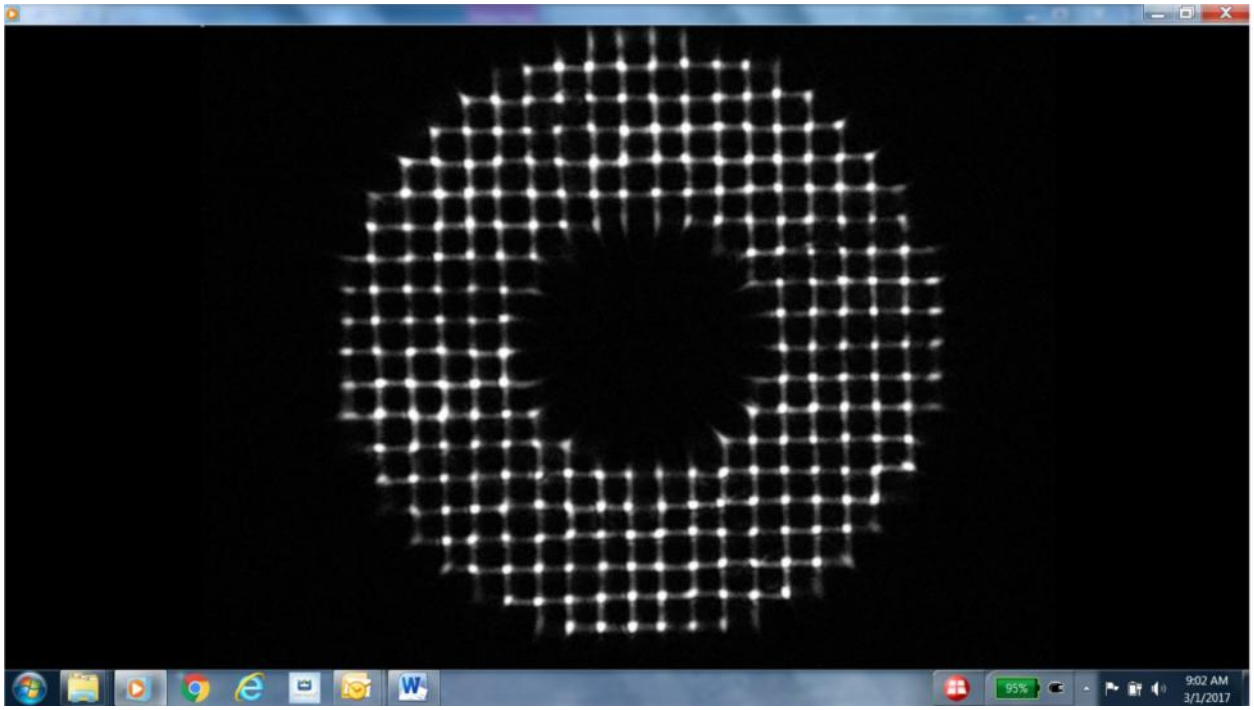


Also, in prior work recorded in Astronomy Notebook Section VI, page 75 titled: Processing of S-H Focal Plane To Give Centroids, dated 3/14/2015, Page 75, Figure 1, shows these lines in the accumulated average for 50 frames.

Coincidently, and not documented in the astronomy notebooks, I notice that reconstruction slope discrepancy deteriorates in the presence of high scintillation.

This entry of the Astronomy Notebook investigates the effect of these lines upon slope centroids. The cause is thought to be the lenslet's rectangular aperture diffraction pattern, which may produce subaperture intensity cross couplings from adjacent subapertures.

There is literature relating to this study. Tory Ellis [1] notes in his USAF dissertation that Shack Hartmann sensors "have problems" in the presence of scintillation and "can severely limit the effectiveness of applications such as the Airborne Laser (ABL). Similarly, Barchers [2,3]

characterizes the performance of S-H sensors in strong scintillation. Plett [4] studies S-H sensor error vs spot width and incident intensity and concludes that the intensity dynamic range (scintillation) makes the sensor susceptible to camera noise for low intensities, and susceptible to pixel saturation at high intensities. Additionally, he notes that there is an optimal spot size.

## 2. Shack Hartmann Sensor Vrsn 2

In this study a second version of the Shack Hartmann sensor is used. This second version superimposes the telescope's blur spot in the middle of the array of Hartmann spots. In this way only one focal plane senses both the Hartmann spots and the telescope blur spot and avoids the synchronization and data rate problems of what otherwise would be two focal planes. Matrix ray trace diagrams of the two optical paths are shown below. Common optics of the two paths are the telescope's primary/secondary mirrors, reimaging Lens2, and projection Lens 5

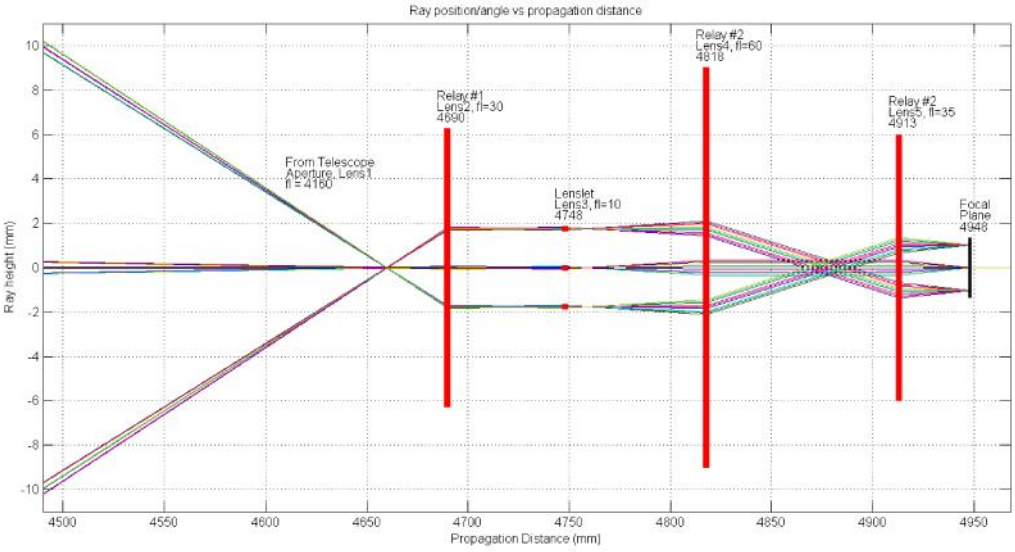


The first relay pair uses the telescope's primary/secondary mirrors along with Lens2 to relay the telescope's entrance pupil to the lenslet array. A second relay pair consisting of lens L4, and L5 relays and rescales the lenslet array's blur spots to fit on the smaller focal plane. These two relay systems form the first optical path.

The second optical path bypasses the lenslet array of the first optical path with a beamsplitter at 4719 mm distance along the optical path. After bypassing the lenslet array the two optical paths are merged with a second beamsplitter inserted at 4847 mm distance along the optical path. This second path uses a third relay pair consisting of L6,and L7 to relay the optical wavefront seen at lenslet array L3's front focal point to the front focal point of L5, thereby rejoining the first optical beam path's Hartman spots.

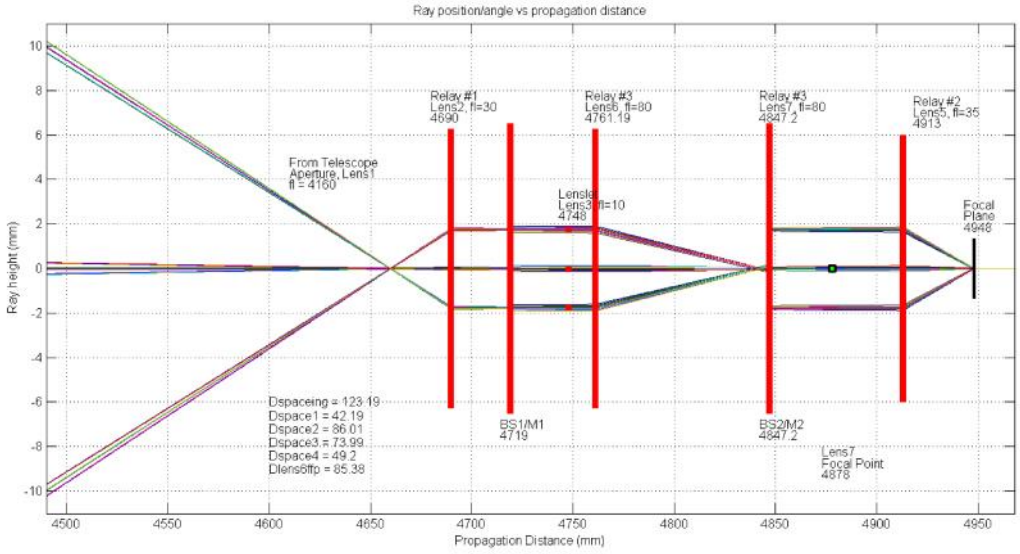


In this way, both the telescope's native blur spot and the Hartmann array spots are imaged on the same focal plane. While the intent is to correlate the two, since the blur spot is the Fourier transform of the wavefront reconstructed from the Hartmann spots, only the first path, that of the Hartmann spots, is used in this study.

# 3. Calculations

## 3.1 Point Spread Functions

The nature of the diffraction pattern is checked by calculating the point spread function of the rectangular lenslet subapertures. Lenslets are on 190 micron centers with focal distances of 10 mm, i.e., each lenslet f/# is $10\text{mm} \div 0.190\text{mm} = 52.6$. Of concern is the proper treatment of the second relay optics L4, L5 that transfer the lenslet spot array from Lens3 back focal point to the focal plane. The lecture from Opti512-29, 13:55 gives the closed form expression of the Airy disk as related to the numerical aperture (NA) of the beam of light at the focal plane. To the question of why use the same Airy disk expression for infinite and finite conjugate optical systems, Dr Masud Mansuripur notes that "what matters is the shape of the beam at the exit pupil. In the case of a collimated beam (infinite conjugate) at the input the spherical wave goes to the focal point. In the case of a finite conjugate lens the spherical wave propagates to an image point that is beyond the focal point. So instead of using $f_o$ (as for infinite conjugation) we would have to use $z_2$".

Thus, because of the magnification of S-H relay lens pair 2 ( Lens4, fl=60mm and Lens5, fl=35mm), the focal plane image from lenslet Lens3 is relayed to the focal plane at the Lens5 back focal distance. The beam numerical aperture (NA) seen at the focal plane is the NA of

lenslet Lens 3 (fl=10mm, d=190 microns) times the demagnification of relay lens pair Lens4 and Lens5. The NA of lenslet Lens3 is,

$$NA_{Lens3} = \sin(\theta_3) = \frac{\frac{d_3}{2}}{f_3} \approx \frac{\frac{0.190\ mm}{2}}{10\ mm} = 0.00950$$

Relay pair demagnification is

$$M_{5,4} = \frac{f_5}{f_4} = \frac{35\ mm}{60\ mm} = 0.5833$$

Thus the NA of the beam incident on the focal plane is,

$$NA_5 = \frac{NA_{lens3}}{M_{5,4}} = \frac{0.0095}{0.5833} = 0.01629$$

From lecture Opti512-27, 43:38 the focal plane image is

$$2\mathrm{NA}_5 e^{-i\frac{\pi}{4}\sqrt{f_o}}\mathrm{sinc}(2\pi\mathrm{NA}_5\,\bar{x})$$

Substituting into the sinc argument we find the first null at,

$$2\pi NA_5\bar{x} = \pi$$

with succeeding lobes at $\frac{3\pi}{2}, \frac{5\pi}{2}, \cdots$, where $\bar{x}$ is $x$ normalized by $\lambda$, i.e., $\bar{x} = \frac{x}{\lambda}$, so that $x \Rightarrow \lambda\bar{x}$ and,

$$x_{1st\ null} = \frac{\lambda}{2NA_5}, \quad x_{1st\ lobe} = \frac{\frac{3}{2}\lambda}{2NA_5}, \quad x_{2nd\ lobe} = \frac{\frac{5}{2}\lambda}{2NA_5}.$$

Parenthetically, since $NA = \sin\theta = \frac{\frac{D}{2}}{f}$, the above equations are equivalent to the more familiar form for the first null,

$$x = \frac{\lambda}{2\left(\frac{\frac{D}{2}}{f}\right)} = \frac{\lambda}{D}f$$

The wavelength $\lambda$ in the above equation is determined by the optical bandpass of this S-H sensor's beamsplitters. The first beamsplitter that separates the relayed beam into two paths is a Thorlabs BSN10 - Ø1" 10:90 (R:T) UVFS Plate Beamsplitter, Coating: 400-700 nm, t = 5 mm. The second beamsplitter that recombines the two beams is a Thorlabs BSW26R - 25 mm x 36 mm 50:50 UVFS Plate Beamsplitter, Coating: 350 - 1100 nm, t = 1 mm. It is seen that the combined transmission of the two is limited by the bandpass of the first beamsplitter, i.e., a wavelength range from 400 to 700 nm.

Since lenslet grid spacing is square with $190 \times 10^{-6}$ meters on a side, its projection on the focal plane with the relay demagnification of $M_{5,4} = 0.5833$ is $M_{5,4} \times 190 \times 10^{-6}\text{meters} = 0.5833 \times 190 \times 10^{-6}\text{meters} = 110.8 \times 10^{-6}\text{meters}$. Of interest is how extensively does the diffraction pattern spill over into neighboring subapertures, and to that end the diffraction pattern's lobes are calculated. The spacings of diffraction lobes for different wavelengths are,

**For $\lambda = 0.4$ microns**

$$x_{1st\ null} = \frac{\lambda}{2NA_5} = \frac{0.4\times10^{-6}}{2\times0.01629} = 12.28 \text{ microns}$$
$$x_{1st\ lobe} = \frac{\frac{3}{2}\lambda}{2NA_5} = \frac{\frac{3}{2}\times0.4\times10^{-6}}{2\times0.01629} = 18.42 \text{ microns}$$
$$x_{2nd\ lobe} = \frac{\frac{5}{2}\lambda}{2NA_5} = \frac{\frac{5}{2}\times0.4\times10^{-6}}{2\times0.01629} = 30.69 \text{ microns}$$

**For $\lambda = 0.5$ microns:**

$$x_{1st\ null} = \frac{\lambda}{2NA_5} = \frac{0.5\times10^{-6}}{2\times0.01629} = 15.35 \text{ microns}$$
$$x_{1st\ lobe} = \frac{\frac{3}{2}\lambda}{2NA_5} = \frac{\frac{3}{2}\times0.5\times10^{-6}}{2\times0.01629} = 23.02 \text{ microns}$$
$$x_{2nd\ lobe} = \frac{\frac{5}{2}\lambda}{2NA_5} = \frac{\frac{5}{2}\times0.5\times10^{-6}}{2\times0.01629} = 38.36 \text{ microns}$$
$$x_{3rd\ lobe} = \frac{\frac{7}{2}\lambda}{2NA_5} = \frac{\frac{7}{2}\times0.5\times10^{-6}}{2\times0.01629} = 53.71 \text{ microns}$$

**For $\lambda = 0.7$ microns**

$$x_{1st\ null} = \frac{\lambda}{2NA_5} = \frac{0.7\times10^{-6}}{2\times0.01629} = 21.48 \text{ microns}$$
$$x_{1st\ lobe} = \frac{\frac{3}{2}\lambda}{2NA_5} = \frac{\frac{3}{2}\times0.7\times10^{-6}}{2\times0.01629} = 32.23 \text{ microns}$$
$$x_{2nd\ lobe} = \frac{\frac{5}{2}\lambda}{2NA_5} = \frac{\frac{5}{2}\times0.7\times10^{-6}}{2\times0.01629} = 53.71 \text{ microns}$$

To test for cross coupling between adjacent subapertures a Matlab program was written that forms a blur spot from the superposition of sinc(x) functions for the wavelengths 400, 450, 500, 550, 600, 650, 700 nm.

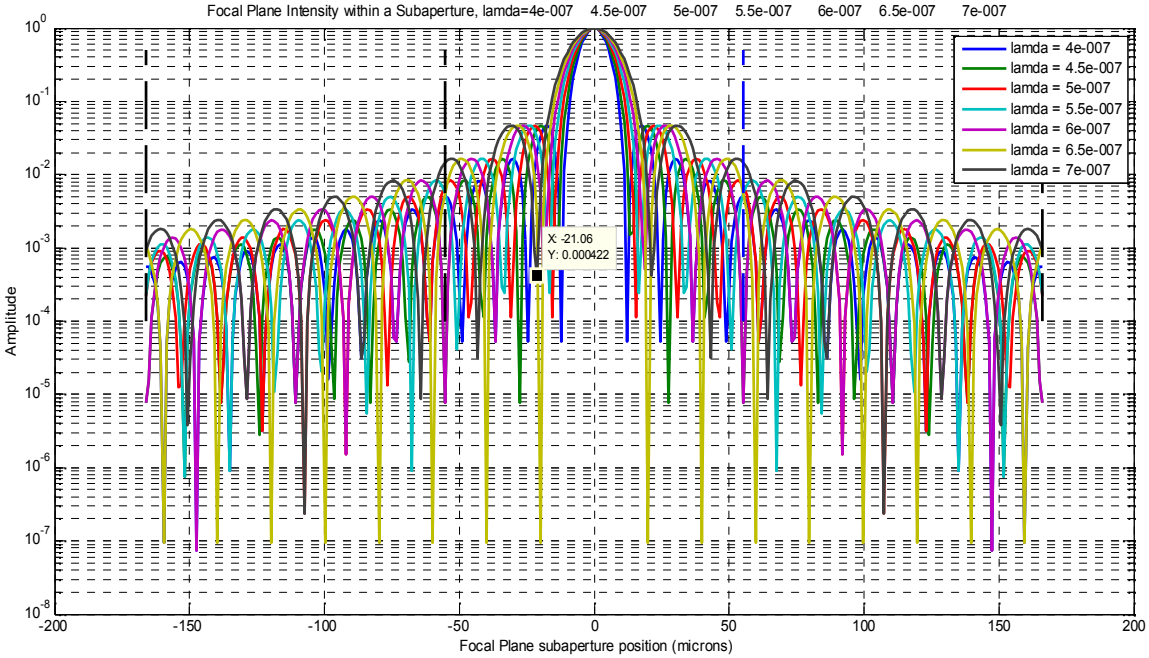


The simulated focal plane blur spot is a superposition of a rectangular aperture's sinc functions at different wavelengths. Vertical black dashed lines denote subaperture boundaries on the focal plane of width 110.8 microns.

The summed intensity is shown in the next figure. It is seen that the centroid contribution to neighboring subaperture intensity is very low, maximizing at 0.006 at subaperture edge and dropping to 0.0004 into the neighboring subaperture's far edge.

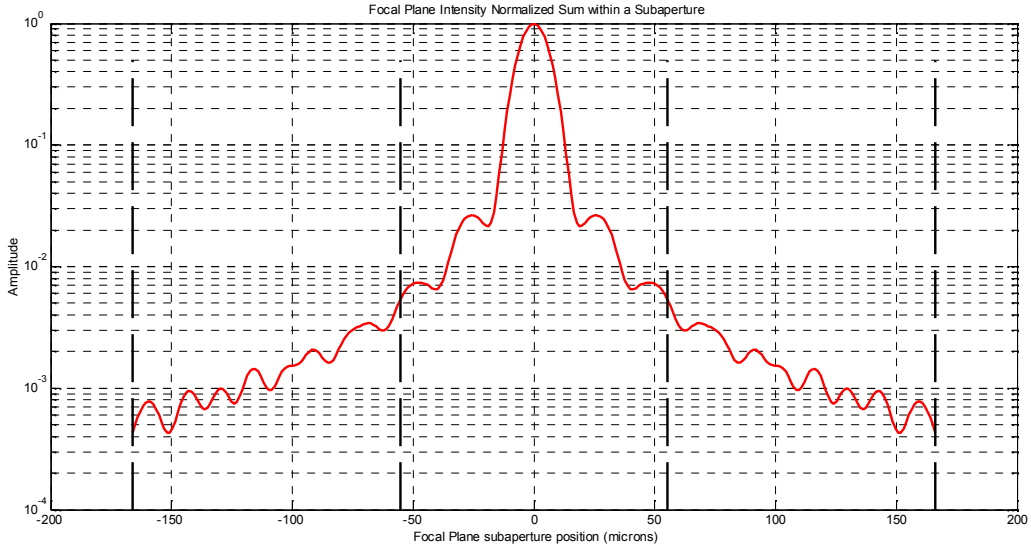

## 3.2 Effect of subaperture jitter

Since blur spot intensity at the focal plane drops with distance from blur spot center, it is desirable to calculate subaperture worst case blur spot displacement to find the worst case coupling from a neighboring blur spot. If jitter brings a neighboring subaperture's blur spot closely to its subaperture edge, then its coupling is stronger. To that end subaperture blur spot jitter at the focal plane is found for the measured atmospheric turbulence Fried's coherence length $r_o$ .

Fried coherence length $r_o$ at the observatory ranges from 4 cm to 15 cm. Using measured $r_o$ the single axis mean-square angular tilt, in units of radians squared [Hardy, pg 121, eq 4.58] is

$$\sigma^2 = 0.182 \left(\frac{D}{r_o}\right)^{\frac{5}{3}} \left(\frac{\lambda}{D}\right)^2$$

where $D$ is the observatory's telescope aperture of 0.5 meters, and $\lambda$ is the wavelength, approximated here as an average of 0.5 microns. Substituting for minimum $r_o$ of 4 cm gives the maximum tilt variance at the telescope entrance pupil,

$$\sigma^2 = 0.182 \left(\frac{0.5}{0.04}\right)^{\frac{5}{3}} \left(\frac{0.5^{-6}}{0.5}\right)^2 = 12.26 \times 10^{-12} \text{ radians}^2$$

or $3.5 \times 10^{-6}$ radians rms. The calculation of subaperture variance follows next, where the prior calculation for the entire aperture tilt showing the dependence of aperture upon tilt variance.

The entrance pupil subaperture spacing is $d = \frac{D}{n} = \frac{0.5 \text{ meters}}{20} = 2.5 \text{ cm}$, where $n$, with $n = 20$ is the number of subapertures on a side of the subaperture grid array. The subaperture single axis tilt variance is,

$$\sigma^2 = 0.182 \left(\frac{0.025}{0.04}\right)^{\frac{5}{3}} \left(\frac{0.5^{-6}}{0.025}\right)^2 = 33.26 \times 10^{-12} \text{ radians}^2$$

or $5.77 \times 10^{-6}$ rms radians. Interestingly this tilt variance is $\frac{5.767}{3.5} = 1.65$, or 65% larger than that seen by the full 0.5 meter aperture. To be conservative by considering 3 $\sigma$ tilt jitter values, the $3\sigma$ subaperture tilt jitter value is 17.3 micro radians at the telescope entrance pupil.

Between the telescope entrance pupil and the lenslet array Lens3 (fl=10 mm) is Lens2 (f=30 mm), which along with the telescope's primary/secondary mirrors, denoted Lens1 (fl=4160 mm), forms the first relay pair with tilt magnification $M_{2,1} = \frac{4160 \text{ mm}}{30 \text{ mm}} = 138.7$. As described in Section 3.1, a second relay pair comprised of lens L4 ($f_4 = 60$ mm) and L5 ($f_5 = 35$

mm), gives demagnification $M_{5,4} = \frac{35}{60} = 0.5833$ and relays the lenslet spot array onto the smaller focal plane. The jitter displacement seen at the focal plane is therefore,

$$3\sigma_{fp} = 3\sigma_{r_o} M_{2,1} f_3 M_{5,4}$$

$$3\sigma_{fp} = 17.3 \times 10^{-6} \text{radians} \times 138.7 \times (10 \times 10^{-3} \text{meters}) \times 0.5833$$

$$3\sigma_{fp} = 14.0 \text{ microns}$$

The focal plane intensity distribution at these displacement extremes are shown below with the nominal distribution shown in red, and the intensity distributions at $3\sigma_{fp} = \pm 14.0$ microns shown in blue. The figure shows that the intensity distributions seem to be well contained within their subaperture.

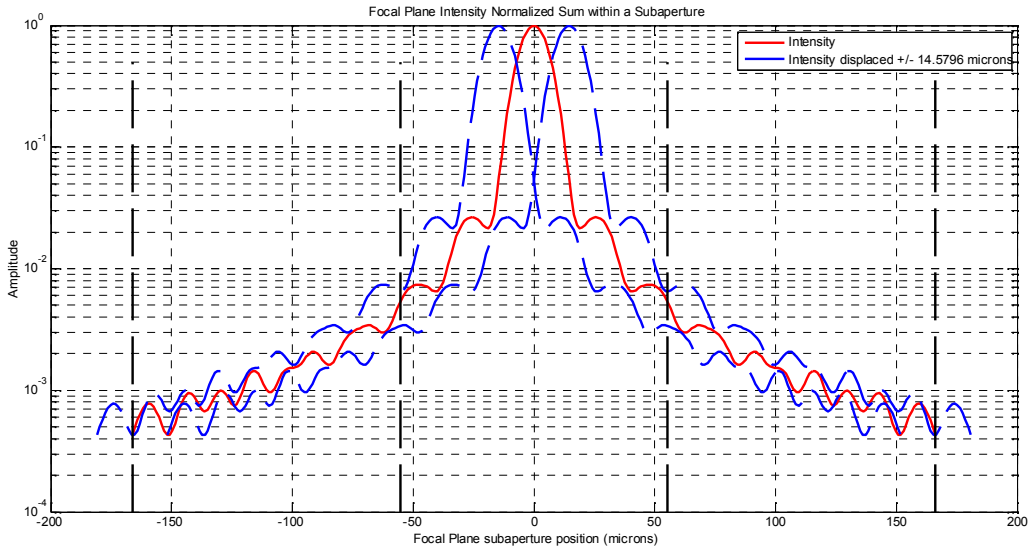


## 3.3 Neighboring subaperture tilt correlation

Neighboring subaperture distributions (not shown) above will have identical blur spot distribution extremes, but their movements will be correlated. By using atmospheric turbulence structure functions, the optical phase variance for spatial separations $r$ that relates wavefront phase $\phi(r)$ is,

$$D(r) = E\{[\phi(r) - \phi(0)]^2\} = 6.88\left(\frac{r}{r_o}\right)^{\frac{5}{3}}$$

with units of radians squared. Since $\left(\frac{\lambda}{2\pi}\right)\sqrt{D(r)}$ is the optical path difference (OPD) over displacement $r$ in radians, then for a subaperture spacing $r = d$ the wavefront's angular slope difference $\zeta$ in radians between adjacent subapertures at the telescope entrance pupil is

$$\xi = \tan^{-1}\left(\frac{\left(\frac{\lambda}{2\pi}\right)\sqrt{D(d)}}{d}\right) \approx \frac{\left(\frac{\lambda}{2\pi}\right)\sqrt{D(d)}}{d}$$

where again $d$ is subaperture spacing, and the approximation follows because the slope difference angle over distance $d$ is small and the tangent of a small angle is approximately the angle itself. The relative blur spot to blur spot displacement difference seen at the focal plane is therefore,

$$\xi_{fp} \simeq \xi M_{2,1} f_3 M_{5,4}$$

For this application with minimum $r_o = 4$ cm and subaperture spacing $d = 2.5$ cm, the atmospheric turbulence induced phase variance between adjacent subapertures is,

$$D(r) = E\{[\phi(r) - \phi(0)]^2\} = 6.88\left(\frac{2.5\text{ cm}}{4\text{ cm}}\right)^{\frac{5}{3}}$$

$$D(2.5\text{ cm}) = 3.14\text{ radians}^2$$

or $\sqrt{D(2.5\text{ cm})} = 1.77$ radians rms. The subaperture to adjacent subaperture OPD is therefore,

$$OPD = \left(\frac{\lambda}{2\pi}\right)\sqrt{D(2.5\text{ cm})}$$

$$OPD = \left(\frac{0.5\times10^{-6}\text{ meters}}{2\pi\text{ radians}}\right)\ 1.77\text{ radians rms}$$

$$OPD = 0.1409 \times 10^{-6}\text{ meters rms}$$

The subaperture-to-subaperture differential OPD tilt angle is therefore $\frac{OPD}{d} = \frac{0.1409\times10^{-6}\text{meters}}{2.5\times10^{-2}\text{meters}} =$ 5.6 urad. The relative blur spot to blur spot displacement difference seen at the focal plane is therefore,

$$\xi_{fp} = \xi M_{2,1} f_3 M_{5,4}$$

$$\xi_{fp} = 5.6 \times 10^{-6}\text{radians} \times 138.7 \times (10 \times 10^{-3}\text{meters}) \times 0.5833$$

$$\xi_{fp} = 4.53\text{ microns}$$

To be conservative, one might consider the 3 sigma value of relative subaperture-to-subaperture blur spot displacement of $3\xi_{fp}$ or 13.6 microns.

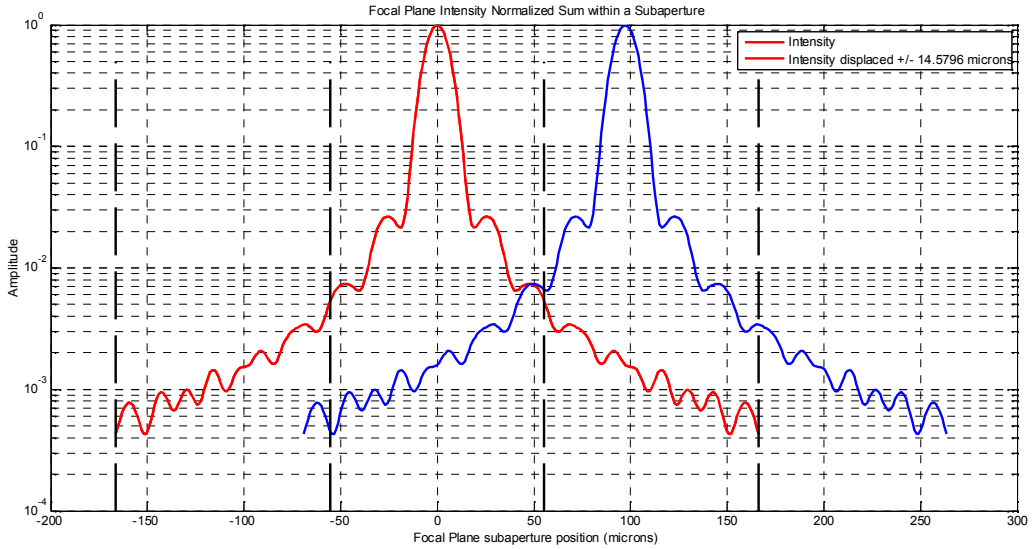


## 3.4 Effect of Scintillation

The Earth's turbulent atmosphere causes stars to "twinkle", i.e., to undergo rapid fluctuations in their measured intensity as seen on the ground. These are "flying shadows" that change their shape and intensity quickly over time and are labelled as scintillation. Scintillation is produced mostly by wavefront curvature [5], because it involves focusing and defocusing within the optical wavefront. For astronomical viewing, whose line of sight extends through the entire atmospheric, scintillation originates in the upper atmosphere.

The figure below shows this telescope's (0.5 meter aperture) entrance pupil Hartmann spots that have scintillation induced intensity variation. The center spot is the relayed telescope point spread function from optical path 2 (see Section 2) and is not relevant to this analysis.

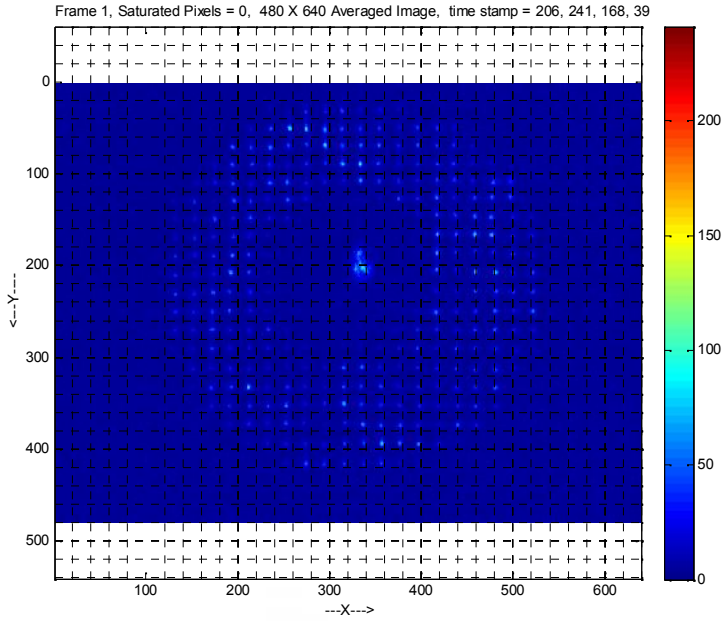


Each S-H blur spot has scintillation induced intensity differences and are the "flying shadows" [5] that sweep across the telescope aperture with time. The amount of scintillation is quantified by the scintillation index $\sigma_I^2$ as defined [6, 7] by the normalized variance of fluctuations in intensity $I$,

$$\sigma_I^2 = \frac{var(I)}{mean(I)^2}$$

For small scintillation index values $\sigma_I^2 \leq 0.1$ the intensity probability density function approximates as Gaussian, but tends to a Poisson distribution shape for larger $\sigma_I^2$ [5].

In some publications [6] the intensity variance is instead given for the logarithm of measured intensity,

$$\sigma_{I_{\ln(I)}}^2 = \left[e^{\sigma_{ln(I)}^2} - 1\right]$$

which equals $\sigma_I^2$ [6] for weak scintillation and obeys a more Gaussian probability density function distribution. This distribution follows from the theory that random perturbations in the propagation path have a multiplicative effect, and the logarithm of these perturbations are additive. Over an appreciable propagation path the number of multiplicative effects becomes large, and from the central-limit theorem the sum of these logarithmic perturbations gives a Gaussian distribution.

For small scintillation index values $\sigma_I^2 \leq 0.1$ both measurement formulations give similar index values.

Of interest in this cross coupling study is the ratio of intensities between adjacent subapertures. If scintillation produces a smaller subaperture intensity vis a vis its neighbor, then

the neighboring subaperture couples more strongly and potentially produces subaperture centroiding error. To that end the log normal distribution is useful because the intensity max/min ratio is simply the antilog of the difference in log intensities. Further, since the log intensity is mostly a normal distribution probabilities may be assigned. Thus the standard deviation of the log variance is,

$$\sigma_{\ln(I)} = \sqrt{\ln\left(\sigma^2_{I_{\ln(I)}} + 1\right)}$$

and the ratio of max to min intensities is the antilog,

$$\frac{I_{max}}{I_{min}} = e^{ln\left(\frac{I_{max}}{I_{min}}\right)} = e^{[ln(I_{max}) - ln(I_{min})]} = e^{\eta\sigma_{\ln(I)}}$$

where the last equality follows from taking the difference in intensity logs as some multiple $\eta$ of the log normal distribution standard deviation $\sigma_{\ln(I)}$ . If $\eta = 2$ for example, then the ratio between maximum and minimum intensities is ± one natural log normal standard deviation.

While the ratio of max to min intensities is found from the log normal distribution $\sigma^2_{I_{\ln(I)}}$, it may also be found from the scintillation index $\sigma_I^2$ xpression for low values of $\sigma_I^2$. Thus, given an intensity probability density function with mean $\mu$ and variance $\sigma^2$, the ratio between the lower bound of greatest intensities $I_{max}$ and the upper bound of the least intensities $I_{min}$ is the ratio between upper and lower regions of the intensity pdf,

$$R_{min}(k) = \frac{\mu + k\sigma}{\mu - k\sigma}$$

where *k* is a constant that scales intensity standard deviation, giving a larger max/min intensity ratio for larger $k$. From the normalized variance version of the scintillation index $\sigma = \mu\sigma_I$, then

$$R_{min}(k) = \frac{\mu + k\mu\sigma_I}{\mu_I - k\mu\sigma_I}$$

$$R_{min}(k) = \frac{1 + k\sigma_I}{1 - k\sigma_I}$$

Thus, if $\sigma_I^2 = 0.1$, i.e, low scintillation for example, then $\sigma_I = 0.3162$ and for $k = 1$, the ratio is 1.92. For moderate to strong scintillation, whose scintillation index values range up to five or six, the above expression's denominator goes to zero and fails to be useful.

## 3.5 The Importance of Thresholding

This section shows the importance of modest thresholding in minimizing adjacent subaperture crosstalk. The motivation comes from the centroiding algorithm itself,

$$C_x = \frac{\sum x(i)\, I(i)}{\sum I(i)}$$

As subaperture position $x(i)$ in the numerator approaches subaperture boundaries, it increasingly weights the contribution of edge intensity, including intensity that spills over from neighboring subapertures. Not uncommonly, scintillation produces subaperture intensity differences between neighboring subapertures, with a ratio of 1:6 for commonly observed scintillation indices ranging upwards of $\sigma_I^2 = 0.4$ . For a 1:6 ratio, the next figure shows the contribution of a neighboring subaperture upon the centroiding process. Thresholding minimizes this centroiding error by reducing the summing interval from ± subaperture edges to a small neighborhood about the subaperture blur spot.

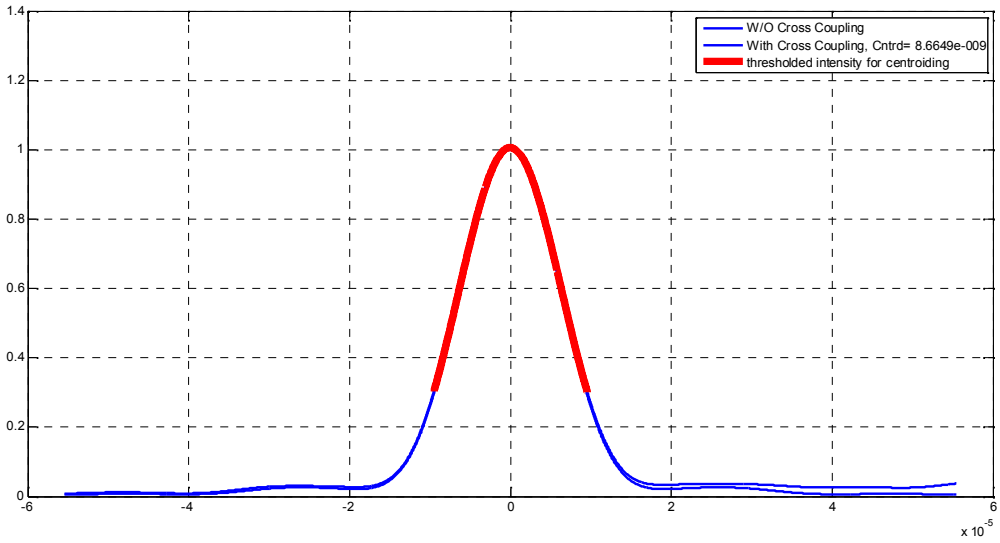


The two traces in blue are the intensity profiles of the subaperture blur spot, and its neighboring right subaperture superimposed contribution. It is seen that while adjacent coupling is small, it is weighted heavily by its large distance $x(i)$ from subaperture center. The red is the thresholded portion of the diffraction pattern. The threshold shown here is 30% of peak amplitude. The centroidng error vs threshold for the 1:6 intensity ratio is shown by the next figure.

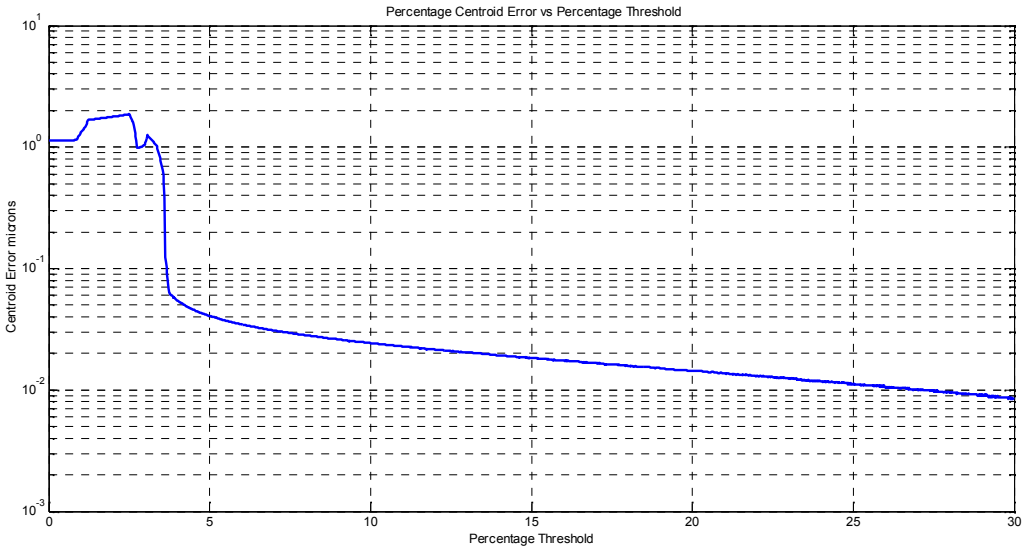


The left most irregular portion of the plot shows that a large centroid error occurs with a zero or very low threshold. This irregularity occurs because of the small intensity irregularities that extend to the ± subaperture boundaries. As the threshold percentage increases there is an abrupt decline of centroiding error as only the main body of the blur spot diffraction pattern contributes to the centroiding.

For thresholding less than 5%, maximum centroiding error is substantial at almost 1.9 microns. At 30% thresholding the centroiding error reduces significantly to only 0.008 microns. Since the blur spot displacement at the focal plane relates to the tilt at the telescope's entrance pupil as,

$$\xi_{fp} = \xi M_{2,1} f_3 M_{5,4}$$

where $M_{2,1} = \frac{f_1}{f_2} = \frac{4160\ mm}{30\ mm} = 139$ is the angular magnification of Relay Pair 1, $f_3 = 10\ mm$ is the focal length of Lens3 lenslets, and $M_{2,1} = \frac{f_5}{f_4} = \frac{35\,mm}{60\,mm} = 0.5833$. The tilt error, which is substantial, seen at the telescope entrance pupil is

$$E_{tilt} = \frac{1.9\times10^{-6}}{139\times10\times10^{-3}\times0.5833} = 2.5 \times 10^{-6} \text{ radians}$$

Similarly, for centroiding error of 0.008 microns the tilt error seen at the telescope entrance pupil is,

$$E_{tilt} = \frac{0.008\times10^{-6}}{139\times10\times10^{-3}\times0.5833} = 0.0106 \times 10^{-6} \text{ radians}$$

which is negligible.

# 4. Experimental Results

## 4.1 Atmospheric Turbulence of Nov 21, 2017

To study the effect of scintillation on subaperture cross coupling movies were made in the observatory of Hartmann spots using the Shack Hartmann (S-H) sensor, version 2. The S-H sensor maps the telescope's aperture of 0.5 meters onto the focal plane as a $20 \times 20$ grid array of Hartmann spots. The focal plane is an 8-bit CCD Point Grey Flea3 model FL3-GE-03S1M-C (Sony ICX618 CCD ¼", 5.6 um chip) operated at 120 fps.

Experimental atmospheric data is in the form of Hartman spot movies of bright star light. Using Vega starlight, the movie data for this experiment was taken on the evening of November 21, 2017. Exposure time is adjusted (5 msec) to exclude focal plane saturation. The particular movie analyzed here (Vega_120fps_5msExp_2017-11-21-184838-0000) has 1000 video frames.

Wind models (www.ventusky.com) show the jet stream at 12,000 meters (39,000 feet) to have a 60 mph wind velocity so scintillation should be moderately strong. Estimated wind velocities and direction at that same time vs altitudes are,

| Altitude (meters) | Wind Speed (mph) | Wind direction |
|---|---|---|
| 500 | 3 | SE |
| 750 | 3 | SE |
| 1,000 | 5 | S |
| 1,500 | 12 | SSW |
| 2,000 | 15 | SSW |
| 2,500 | 15 | SSW |
| 3,000 | 20 | SSW |
| 3,600 | 21 | SW |
| 4,200 | 33 | SW |
| 5,500 | 39 | SW |
| 9,000 | 65 | SW |
| 12,000 | 60 | SW |

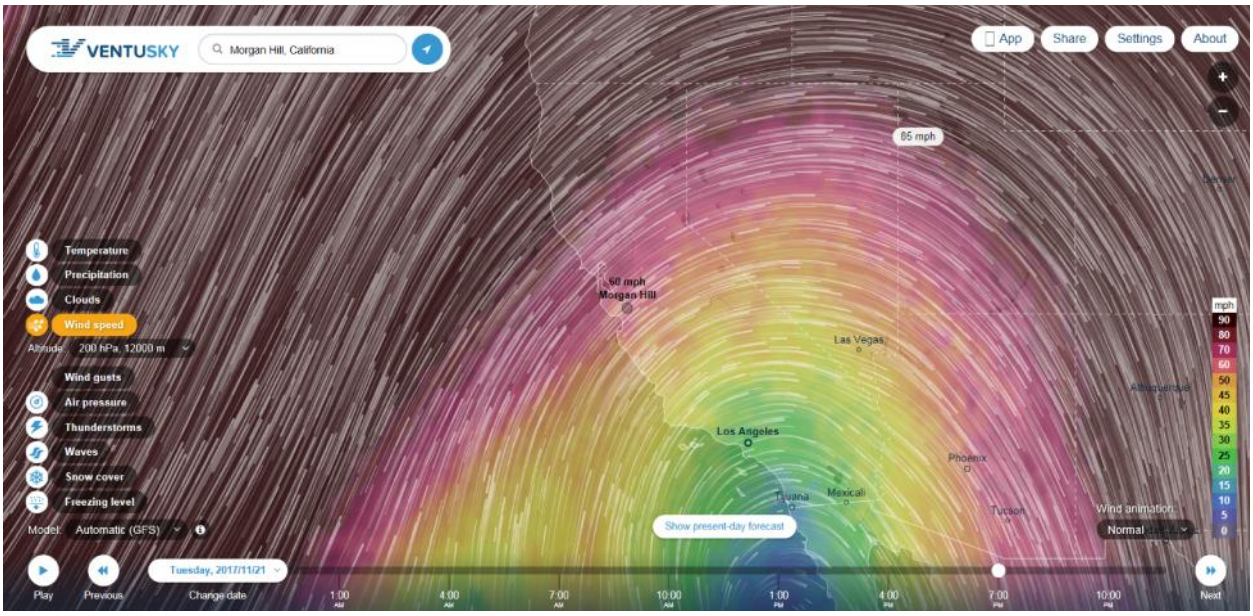


The table shows a natural wind gradient with altitude, with no appreciable crosswinds. It is not uncommon, however, for wind at a higher altitude (the jet stream) to flow orthogonally to winds that flow at lower altitudes within the Santa Clara Valley.

A Matlab centroiding program was written to process the movie data's Hartmann spots. It has the ability for one to selectively turn on or off several figures to monitor the centroiding algorithm's processing. The first figure below of example frame 1 shows the nature of scintillation in which some subapertures are bright, some dark, and others moderately illuminated. These are the 'flying shadows' that stream across the telescope aperture at some velocity. There are no saturated pixels in this data. The central blur spot is ignored in this analysis.

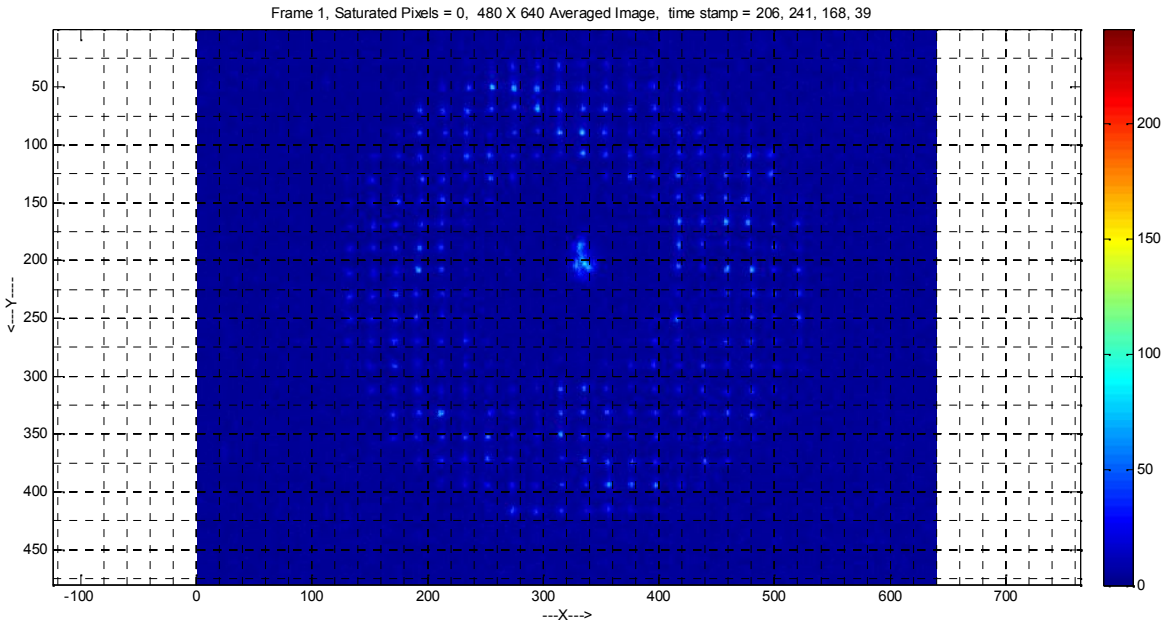

To automatically establish subaperture grid coordinates all the movie frame's Hartmann spots are averaged. Grid coordinate offsets, slopes, and spacings are found in the sense of least squares that fit the averaged spots. The figure below details the averaging and centroiding and is useful because it shows the mean nature of the Hartmann spots without noise.

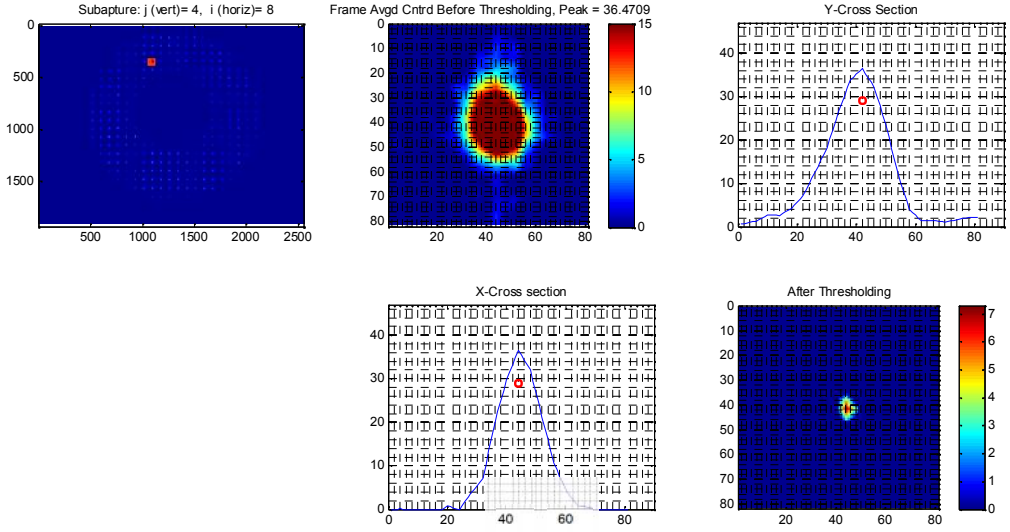


The 1st panel (upper left) denotes the $i^{th}, j^{th}$ subaperture in the Hartmann spot array that is being examined. The 2nd panel (upper center) shows the lower region (0 to 15 ADU counts) of the averaged blur spot, where the diffraction spikes are clearly evident and motivate this study. The 3rd panel (upper right) is the 2nd panel's averaged blur spot's y axis cross section profile, showing the blur spot matches the calculated rectangular diffraction pattern of Section 3.1. The red dot is the dynamic threshold at the y axis centroid, its distance below centroid peak being a programmable percentage of the instantaneous blur spot peak. The 4th panel (lower left) is the averaged blur spot's x axis cross section profile and similarly the red dot shows the dynamic threshold at the x axis centroid. The 5th panel (lower right) is the remaining averaged blur spot after thresholding that is to be centroided. Since this is an all frame average, focal plane noise randomness is averaged out and shows as a baseline mean.

The next figure shows a subaperture's unaveraged, individual centroid intensity as it occurs for example frame 2, at $i^{th}, j^{th}$ subaperture grid position $i = 10, j = 19$.

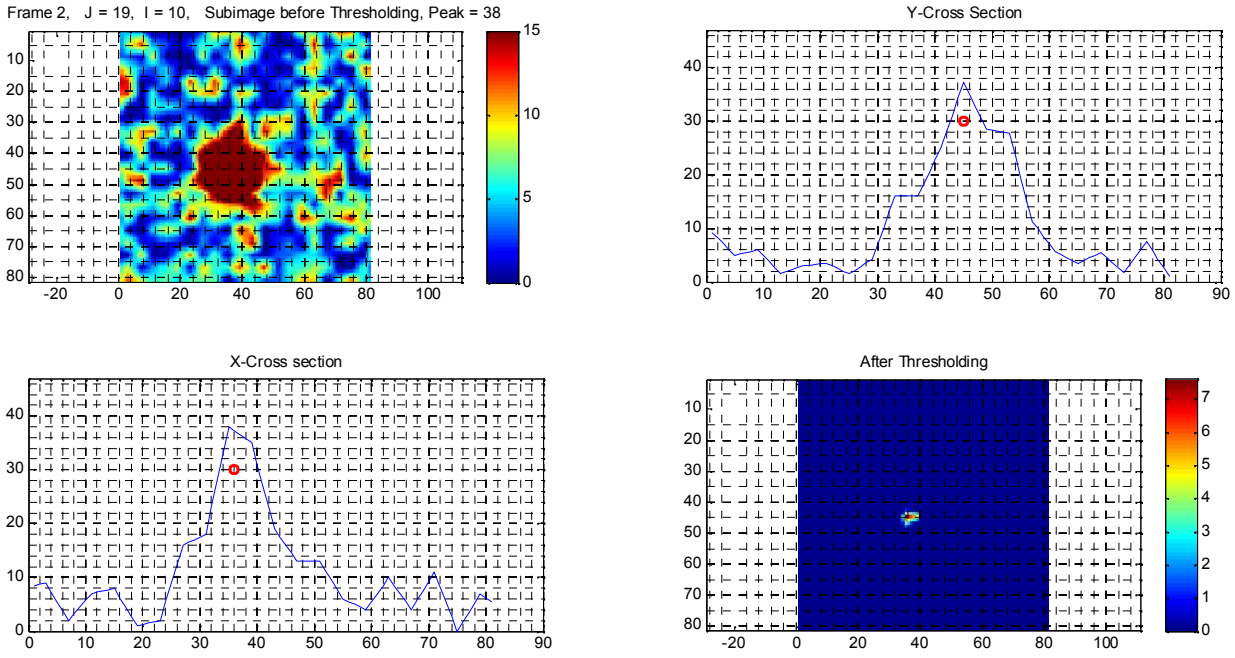


As for the previous figure, The 1st panel (upper left) shows the lower region (0 to 15 ADU counts) of the unaveraged subaperture blur spot, where the diffraction spikes are not seen, being dominated by focal plane noise. Parenthetically, using the Andor Zyla camera with very low noise, this is not the case and diffraction patterns are clearly seen. The 2nd panel (upper right) is the unaveraged blur spot's y axis cross section profile, with a red dot description as before. The 3rd panel (lower left) is the unaveraged blur spot's x axis cross section profile, while the 4th panel (lower right) is the unaveraged blur spot after thresholding that is centroided.

The next figure details the intensity and log intensity histograms of an example (i=12, j=20) subaperture.

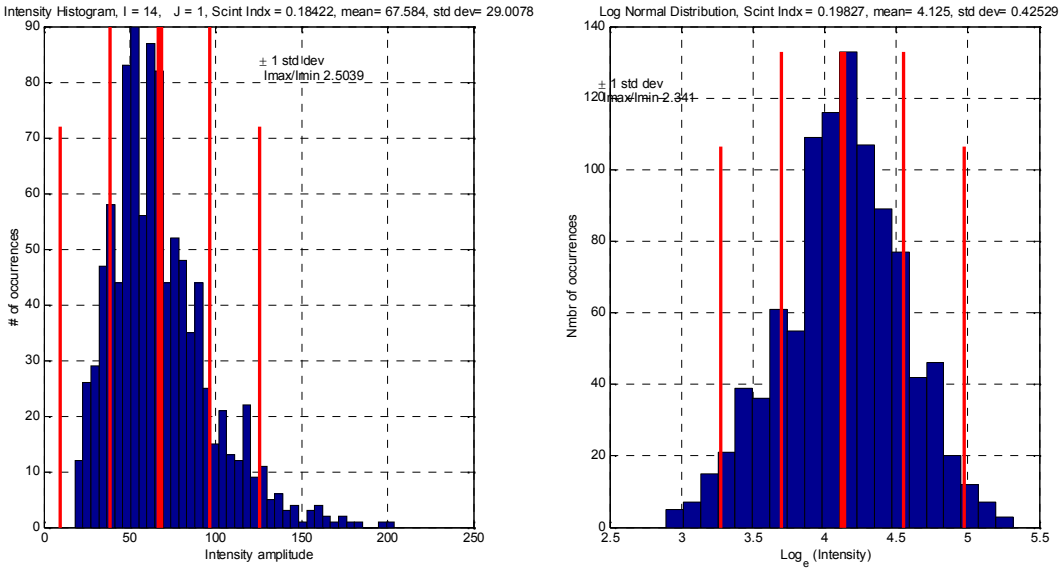

The above histograms show the nature of subaperture intensity and log intensity distributions for an $i^{th}, j^{th}$ subaperture grid position $i = 14,\ j = 1$. In each panel the thick vertical red line is the histogram mean, while the thinner red lines are the $\pm 1\sigma$, and $\pm 2\sigma$ standard deviations from the mean. The intensity histogram panel on the left shows a log-normal distribution (but a more Gaussian distribution for $\sigma_I^2 \leq 0.1$). The log intensity histogram on the right is more Gaussian.

In their respective titles it is seen that the scintillation indices are similar, $\sigma_I^2 = 0.184$ on the left panel and $\sigma_I^2 = 0.198$ on the right as expected [6] because this is weak scintillation. The ratio between -1σ and +σ intensity distributions is 2.5 on the left vs 2.3 for the log normal variance on the right. Note that the left panel's probability density function changes with scintillation index so it is difficult to assign probabilities and hence its -1σ and +σ ratio is not useful.

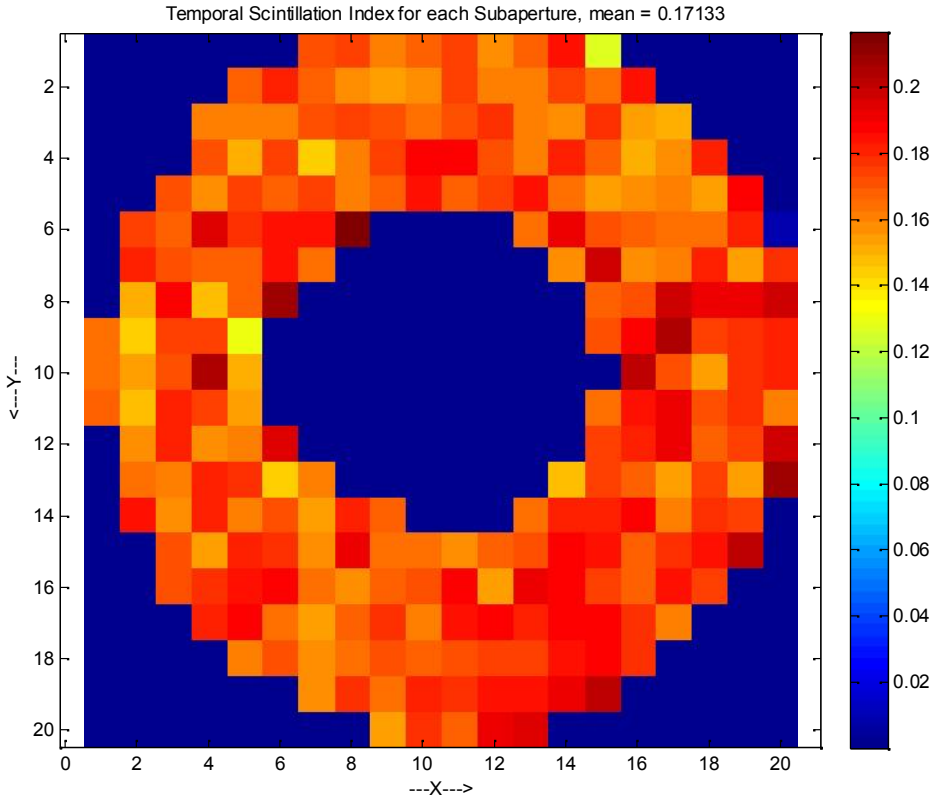


The above figure shows the scintillation index $\sigma_I^2$ for each subapertures with an average mean index of 0.17 across all subapertures. The ratio between greatest and least is about 2:1 and aside from a few edge subapertures is fairly uniform.

## 4.2 Atmospheric Turbulence of Nov 28, 2015

Other atmospheric turbulence data is available for analysis, but doesn't have a Ventusky velocity profile. One such data was taken on the night of November 28, 2015, but with an Andor Zyla 5.5 sCMOS 12-bit USB3.0 camera instead of the 8 bit Point Grey Flea3 model FL3-GE-03S1M-C. Operated in global shutter mode with resolution 512 x 512 and operated at 185 fps, the Zyla camera has measured noise of 2.78 e- RMS. By contrast the Flea 3 camera with resolution 640 x 480 and operated at 120 fps has measured noise of 27.8 e- RMS (See result table on page 3 of Astronomy Notebook, dated June 10, 2016).

The Andor Zyla camera with its improved frame rate, 10X lower noise, and 16X greater dynamic range therefore has better fidelity to measure atmospheric turbulence at higher scintillation values.

Movies were made of the S-H sensor using Capella starlight and the camera was operated at 168 fps, with a 1 millisecond exposure time. The faster exposure time minimizes blurring of the Hartmann spots from an ever changing turbulence aberration. The file name is Zyla_Capella_600frames_168fps_Exps1msec_Global_512x512_2015_11_28.tif and consists of 600 frames. In this data set, the atmosphere exhibited increased scintillation from that of November 17, 2017. An example frame histogram for the $i^{th}, j^{th}$ subaperture grid position $i = 9, j = 4$ shows a scintillation index $\sigma_I^2 = 0.536$ .

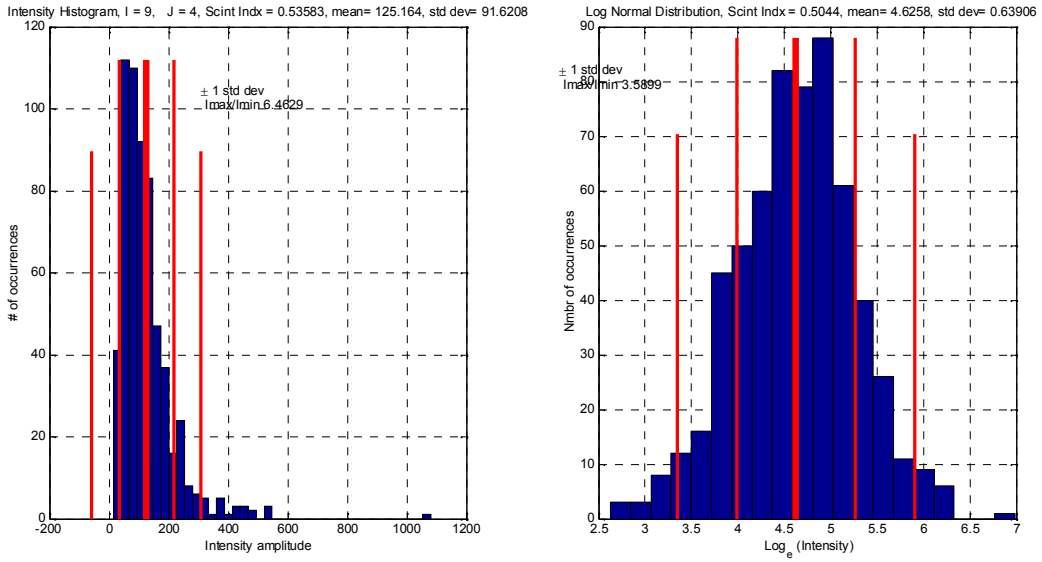


The figure above shows the nature of the intensity histogram distributions. On the left panel the amplitude distribution shows as a log normal distribution with some intensity values very close to zero, with a bright intensity spike out to 1080. The distribution on the right shows that the log of intensity results in an approximate Gaussian distribution as expected. Note that this is only moderately strong scintillation. It is easy to see that strong scintillation $\sigma_I^2$ ranging up to 4 will give moments of light intensity that are less than the focal plane noise floor.

Besides concern for low light levels, there is the problem of the Shack Hartmann's susceptibility to wavefront branch points in which the wavefront E-field phase function has unavoidable $2\pi$ discontinuities. Barchers, Fried and Link [2] find that the performance of Hartmann sensors degrades severely when the Rytov number exceeds $0.2$ . The Rytov variance represents the normalized irradiance variance, or scintillation index $\sigma_I^2$, of a plane wave in weak fluctuations, but is otherwise a measure of optical turbulence strength in strong fluctuation regimes [9, pg 2].

Thus, for the above distribution with $\sigma_I^2 = 0.536$, not only are there problems with light intensity drop-outs, but also problems with E-field $2\pi$ discontinuities or branch points. On the other hand, an atmospheric turbulence with high scintillation is equally likely to have low values of $r_o$ and be undesirable for any astronomical imaging. The turbulence with the above $\sigma_I^2 = 0.536$ had a very poor $r_o = 4.1$ cm .

## 5. Conclusion

1. The lenslet's intensity distribution spills over into adjacent subapertures for this S-H design with subaperture spacing of 2.5 cm. Usually, subaperture spacing is equal to $r_o$, which for this application would be 4 cm and would otherwise make the S-H less susceptible to subaperture coupling.

2. Adjacent subaperture tilt jitter is correlated over a longer spatial interval than the Fried parameter, so blur spot displacement between neighboring subaperture follow each other to some degree. The jitter difference was calculated and cross coupling is noted.

3. Scintillation modulates the coupling between subapertures with a neighboring well illuminated subaperture coupling more strongly than one that is dark. For moderate scintillation of $\sigma_I^2 \leq 0.4$ adjacent subaperture coupling was observed.

4. Thresholding is a very effective way to mitigate subaperture coupling. Without thresholding adjacent subaperture coupling produced a tilt error of $2.5 \times 10^{-6}$ radians. With only 30% of blur spot peak thresholding the error drops dramatically to $0.0106 \times 10^{-6}$ radians.

4. The dominate failure mode for high scintillation $\sigma_I^2$ is not subaperture to subaperture coupling, but intensity dropouts. Low noise focal planes help in this regard.

5. E-field branch points are likely for moderately strong scintillation for which the atmosphere's Rytov number exceeds 0.2.

6. By comparing the turbulence wind velocity of 5.7 mph found in the Appendix with the wind table of Section 4.1, the turbulence layer is estimated to be at 3000 feet, which coincides with the marine layer altitude.

# References


[1] Troy Ellis, "Shack-Hartmann And Interferometric Hybrid Wavefront Sensor," USAF Dissertation, Air Force Institute of Technology, Wright Patterson Air Force Base, Ohio, March 2011.

[2] Jeffrey D. Barchers, David L. Fried, Donald J. Link, Glenn A. Tyler, William Moretti, Terry J. Brennan, and Robert Q. Fugate. "The performance of wavefront sensors in strong scintillation" L. Wizinowich, Peter and Domenico Bonaccini (editors), Adaptive Optical system Technologies II, volume 4839, 2003.

[3] Jeffrey D. Barchers, David L. Fried,, and Donald J. Link. "Evaluation of the performance of Hartmann sensors in strong scintillation", Appl. Opt., 41(6): pg 1012-1021, February 2002.

[4] M. L. Plett et.al., "Measurement error for a Shack-Hartmann wavefront sensor in strong scintillation conditions", SPIE Proceedings, Vol 3433, July 1998, pg 211-220.

[5] Dainis, "Atmospheric Intensity Scintillation of Stars, I. Statistical Distributions and Temporal Properties", Astronomical Society of the Pacific, Vol 109, Feb 1997, pg 173-207.

[6] Andrews and Philips, Laser Beam Propagation through Random Media, pg 112-113, and pg 176-177.

[7] Andrews, Field Guide to Atmospheric Optics , pg 36.

[8] Tyson & Frazier, Field Guide to Adaptive Optics, 2nd ed pg 12.

[9] Andrews, Phillips, Hopen, Laser Beam Scintillation with Applications, SPIE Press, 2001.

[10] Hardy, Adaptive Optics for Astronomical Telescopes,


# Appendix – Evaluation of Atmospheric Data Video

Besides evaluating scintillation, which originates in the atmospheric tropopause at about 10,000 meters, optical wavefront distortion occurs in the lower elevations and there are a number of metrics for evaluating atmospheric turbulence. The first is the Fried coherence parameter $r_o$, followed by slope discrepancy which measures centroiding noise and fitting noise, and the temporal structure function which gives measurement of coherence time (Greenwood frequency) and wind velocity. The Fried coherence parameter is shown first.

The Fried coherence parameter $r_o$ is computed for each frame using the structure function relation,

$$D(r) = E\{[\phi(r) - \phi(0)]^2\} = 6.88\left(\frac{r}{r_o}\right)^{\frac{5}{3}}$$

where a reconstruction matrix applied to the computed centroids gives OPD error (microns), which is converted to phase (radians) using an average wavelength of 0.5 microns. The figure below shows a typical solution for an example frame 2 of Hartmann spots.

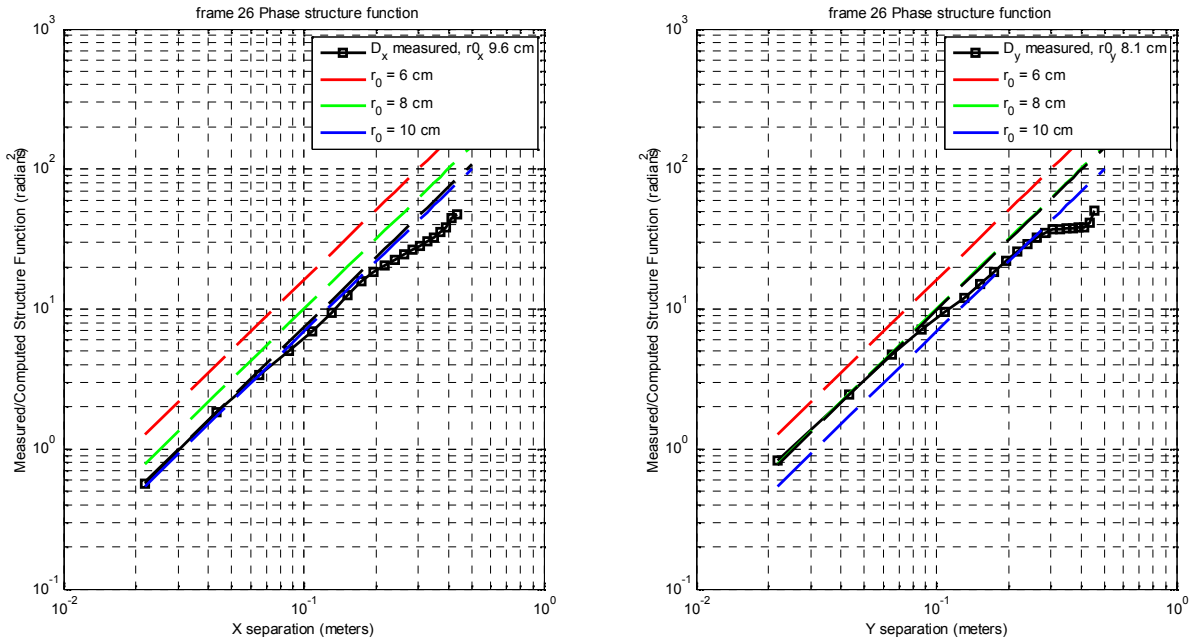


For this frame, while the structure function's log 5/3 relation holds well for spatial intervals less than about 20 cm, it is seen that greater separations have greater variance. Increased variance occurs because there is less averaging as separation distances approach the telescope's aperture diameter. The above structure plot, however, is but one realization of an ensemble of 1000 frames. The 1000 frame expectation is

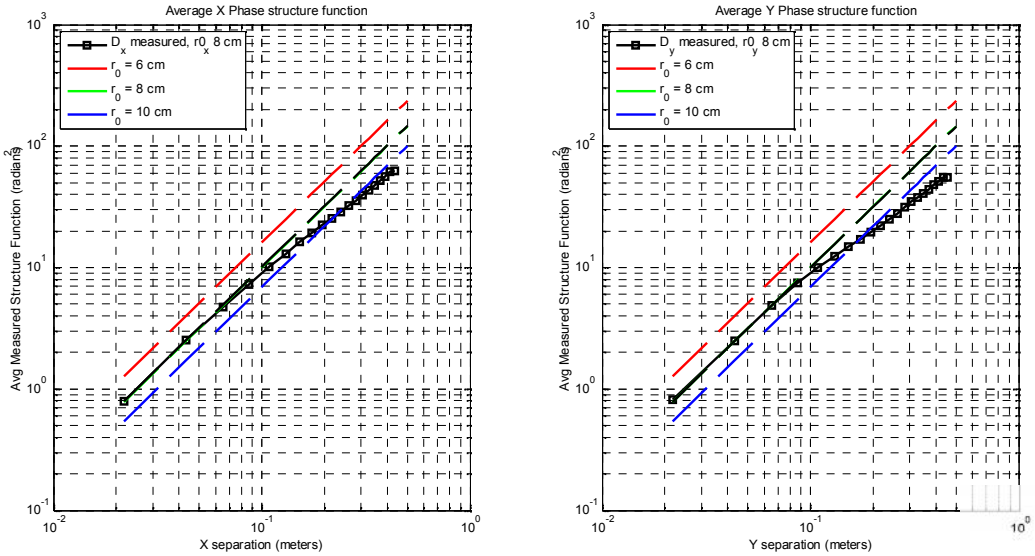


It comparing the two panels above it is seen that ensemble averages for $r_{ox} = r_{oy} = 8$ cm. Thus atmospheric turbulence is isotropic, as expected.

A Hartmann sensor measurement is considered to be an estimate of the mean gradient over the subapertures, but it contains a component that is not in the range space of the operator $\boldsymbol{P}$, this component is called the slope discrepancy, where $\boldsymbol{P}$ is the geometry "poke" matrix. If $\boldsymbol{s}$ is the Hartmann x,y slope column vector. $\boldsymbol{R} = \boldsymbol{P}^{\dagger}$ is the reconstruction matrix, where † denotes the Moore Penrose pseudo inverse, then the reconstructed slope vector is $\boldsymbol{PRs}$ , and the slope discrepancy $\boldsymbol{\delta}$ is the difference between measured and projected slopes,

$$\boldsymbol{\delta = s - PRs}$$

In words, the measurement $\boldsymbol{s}$ is reconstructed with $\boldsymbol{R}$ and projected back into slope space with operator $\boldsymbol{P}$. The difference between this result and the original slope vector is called the slope discrepancy $\boldsymbol{\delta}$ and is in the range space of $\boldsymbol{(I - PR)}$, while $\boldsymbol{g}$ is in the null space of $\boldsymbol{(I - PR)}$.

The slope discrepancy difference as a function of time separation $\tau$ is defined by

$$\Delta_g = \delta(t+\tau) - \delta(t)$$

The slope discrepancy structure function is given by the mean square slope discrepancy difference,

$$E_{\delta}^2(\tau) = \left(\frac{1}{n_s}\right)\langle \Delta_{\delta}(t,\tau)^T \Delta_{\delta}(t,\tau)\rangle$$

The figure below shows the slope discrepancy structure function vs time separation $\tau$, where $\tau$ is a multiple of frame rate sampling interval $T_S$ of 8 msec. It is seen that measurement noise is $\frac{\lambda}{12.4}$ while fitting error is $\frac{\lambda}{36.3}$. See Astronomy Notebook pg 164-166, dated Feb 19, 2016 for details.

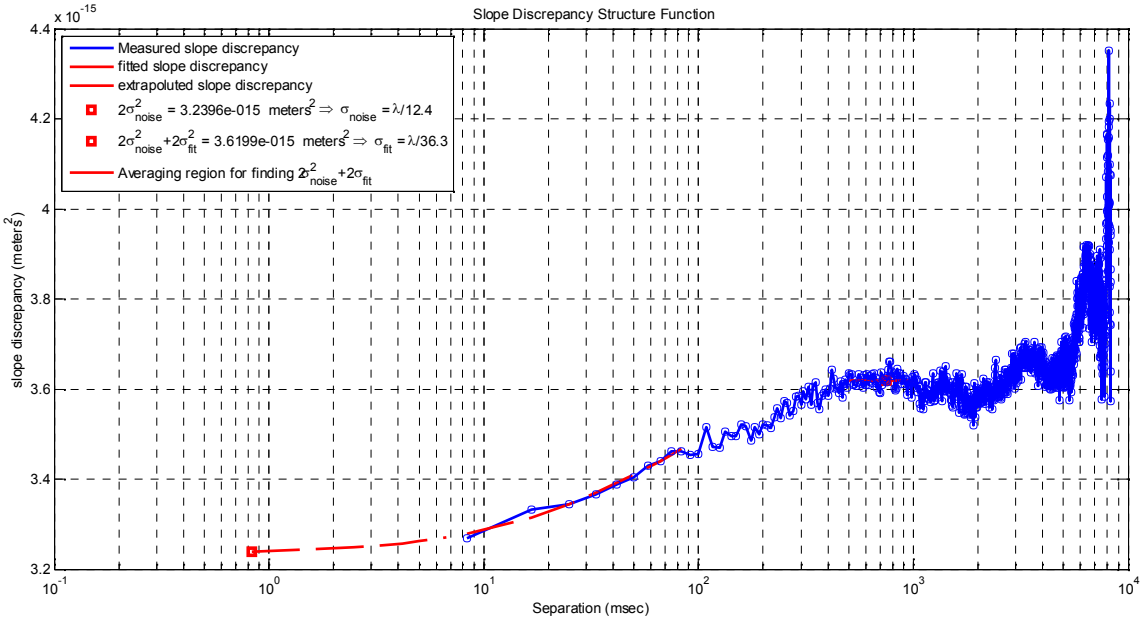


The averaged temporal phase structure function is

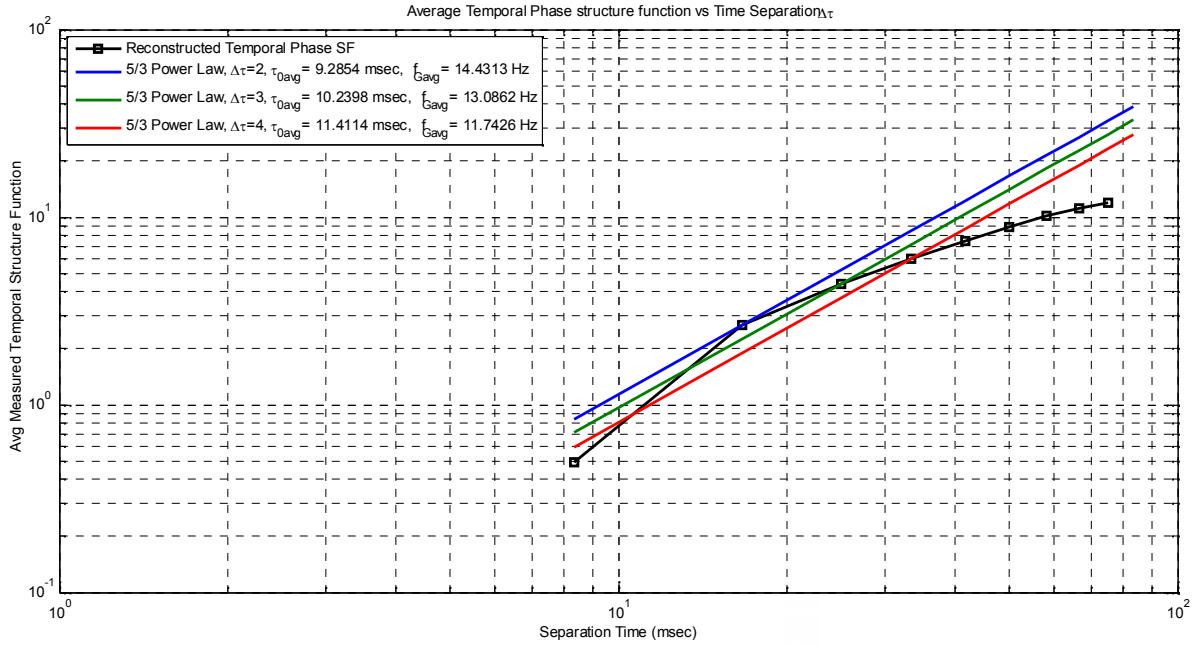


And from the above structure function, the coherence time $\tau_o$ estimate is quite slow ranging between 9.3 and 11.4 msec. Similarly, the Greenwood frequency is also quite low, ranging between 11.7 and 14.4 Hz. This compares with coherence estimates of 5.0 to 6.0- msec and Greenwood frequency of 12.2 to 13.7 Hz on April 24, 2014, recorded in Astronomy notebook, pg 171, dated 2/19/2016. Usual measurements for $\tau_o$ are in the range of 2 to 5 milliseconds, and Greenwood frequencies ranging from 27 to 67 Hz. Greenwood frequency and coherence time are related as, $f_G = \frac{0.134}{\tau_o}$.

From the slope discrepancy, measurement noise estimate and fitting error estimate, the estimated wind velocity for each frame is shown below. The average of all frame estimates is 5.7 miles/hour.

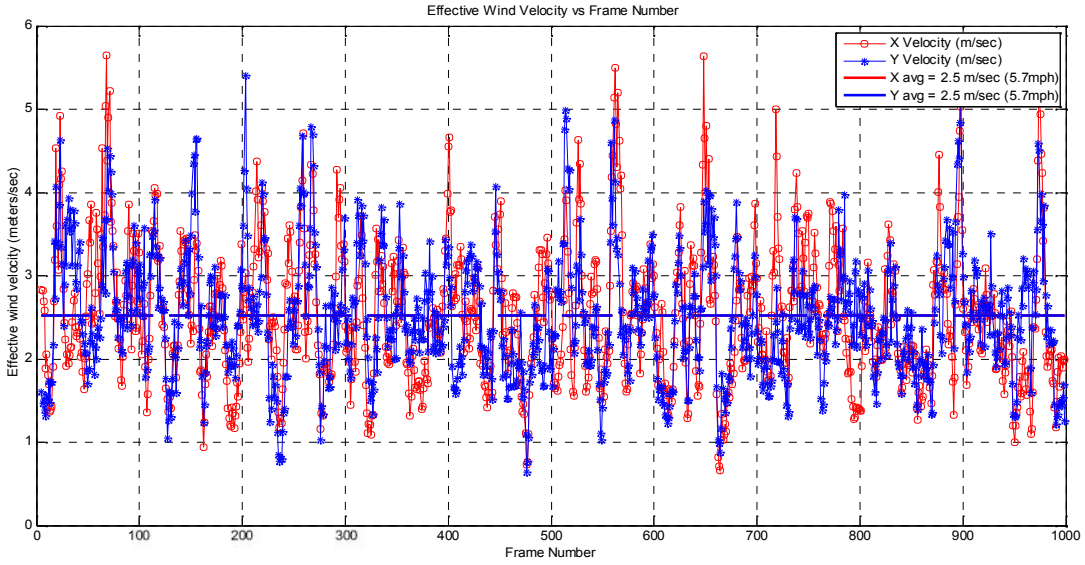


This is a noisy estimate, but averaging is justified because the total time scale for these measurements is $\frac{1000 \text{ frames}}{120 \text{ fps}} = 8 \text{ sec}$ and wind does not change its velocity so rapidly. Using the less noisy Andor Zyla camera may reduce this noise. The estimated wind velocity compares with 10.3 mph on page 173, dated Feb 19, 2016. See Astronomy Notebook pages 166-169, dated Feb 19, 2016 for derivation details of the estimation algorithm